Statistical analysis of electroconvection near an ion-selective membrane in the highly chaotic regime

Clara Druzgalski and Ali Mani

Statistical analysis of electroconvection near an ion-selective membrane in the highly chaotic regime

Clara Druzgalski and Ali Mani

Department of Mechanical Engineering,

Stanford University, Stanford, California 94305, USA and

Center for Turbulence Research, Stanford University, Stanford, California 94305, USA

We investigate electroconvection and its impact on ion transport in a model system comprised of an ion-selective membrane, an aqueous electrolyte, and an external electric field applied normal to the membrane. We developed a direct numerical simulation (DNS) code to solve the governing Poisson-Nernst-Planck and Navier-Stokes equations in three dimensions using a specialized parallel numerical algorithm and sufficient resolution to capture the high frequency and high wavenumber physics. For the first time, we show a comprehensive statistical analysis of the transport phenomena in the highly chaotic regime. Qualitative and quantitative comparisons of 2D and 3D simulations include: prediction of the mean concentration fields, as well as the spectra of concentration, charge density, and velocity signals. Our analyses reveal significant quantitative difference between 2D and 3D electroconvection. Furthermore, we show that high-intensity yet short-lived current density hot spots appear randomly on the membrane surface, contributing significantly to the mean current density. By examining cross correlations between current density on the membrane and other field quantities we explore the physical mechanisms leading to current hot spots. We also present analysis of transport fluxes in the context of ensemble-averaged equations. Our analysis reveals that in the highly chaotic regime the mixing layer (ML), which spans the majority of the domain extent, is governed by advective fluctuations. Furthermore, we show that in the ML the electromigration fluxes cancel out for positive and negative ions, indicating that transport of total salt within the ML can be represented via the electroneutral approximation. Lastly, we present an assessment of the importance of different length scales in enhancing transport by computing the cross-covariance of concentration and velocity fluctuations in the wavenumber space. Our analysis indicates that in the majority of

the domain the large scales contribute most significantly to transport, while effects of small scales become more appreciable in regions very near the membrane.

I.   INTRODUCTION

Ion-selective materials play an essential role in separation and purification processes. For example, in electrodialysis ion-selective membranes are used to purify brackish water. This process can be incorporated into hybrid reverse osmosis systems[1]. Other industries that use electrodialysis include chemical[2], pharmaceutical[3], and food production[4]. Novel applications use ion-selective membranes in redox flow batteries[5, 6] and microfluidics[7] such as biomedical lab-on-a-chip devices, micropumps, and analytical sensors[8, 9].

The aforementioned devices use externally applied electric fields to drive ion transport in aqueous electrolytes. A model setup for a membrane-electrolyte system shown in Figure 1(a), consists of an ion-selective membrane in contact with an electrolyte and a potential difference applied across the domain. When an ion-selective membrane and an electrolyte come into contact, the highly charged membrane surface attracts counterions from the bulk, forming an electric double layer (EDL) adjacent to the membrane surface, see Figure 1(c). The external electric field drives counterions from the bulk fluid to the membrane, and drives coions away from the membrane to the bulk. These effects cause the well-established concentration polarization (CP) phenomenon[10] to deplete both coions and counterions near the membrane surface. The depletion of ions near the interface limits the ability of the system to sustain large electric current. Due to this effect, the measured current versus voltage plots typically saturate at a limiting current, I_{lim}, controlled by diffusion (Figure 2).

For applied voltages much larger than the thermal voltage, V_T, the salt depletion leads to very small concentrations near the membrane and thus singularly large local EDL thicknesses. In this regime, the transition from the EDL to the electroneutral diffusion layer (DL) in the bulk is reconciled via an intermediate layer called the extended space charge region (ESC) which is neither electroneutral nor in Boltzmann-equilibrium. The ESC can be predicted by one-dimensional theories, and allows for a small amount of overlimiting current (OLC). Experimental measurements however, typically reveal OLC values significantly larger than those predicted by the one-dimensional ESC models[11]. Rubinstein and Zaltzman used linear stability analysis of similar systems and showed that beyond a

threshold voltage, the one-dimensional solution to the ESC is unstable, resulting in a hydrodynamic instability referred to as the electroconvective instability (ECI). Based on their analysis, Rubinstein and Zaltzman hypothesized that flow vortices induced by this instability can enhance ion transport via convection and result in OLC. This analysis was confirmed by experimental observation of induced vortices, called electroconvective vortices, near an ion-selective membrane[12].
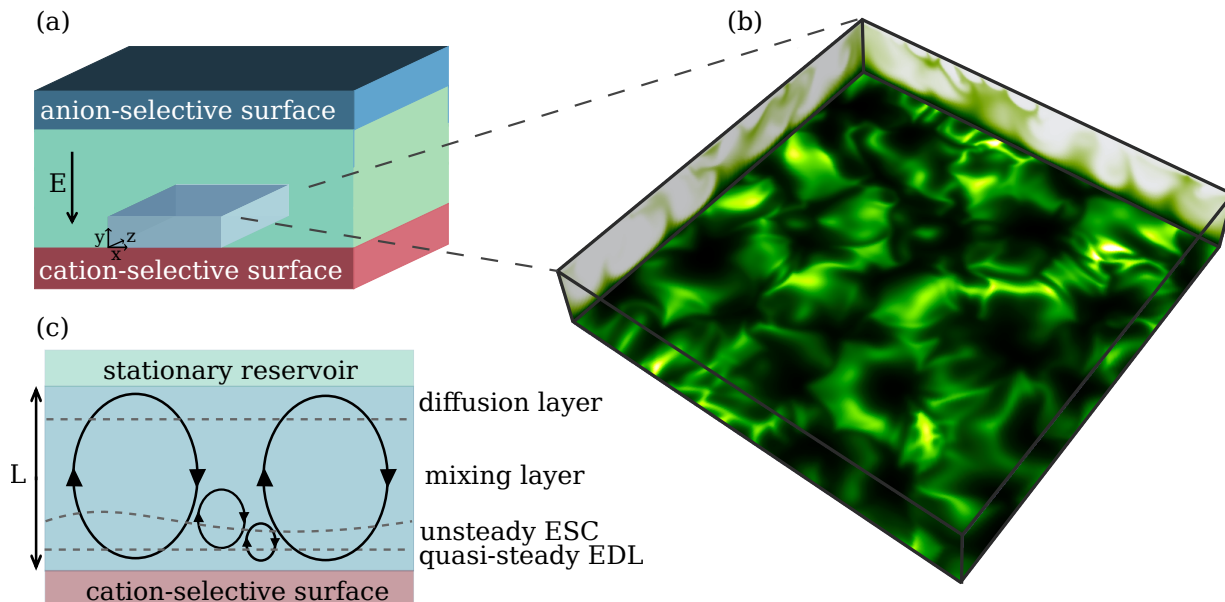
Figure 1. (a) 3D schematic of an electrodialysis device with alternating anion-selective and cation-selective surfaces. (b) An instantaneous snapshot of the chaotic concentration field from our 3D DNS. (c) Schematic of a model system focusing on the physics adjacent to the cation-selective surface. As a result of induced convection, a mixing layer (ML), with an almost flat average concentration profile develops in a large part of the domain.

Recent experimental observations[13–16] revealed that when the applied field exceeds a threshold of $\mathcal{O}(1)$V in aqueous systems, the ion transport generates highly unsteady fields of fluorescent signals representing ion concentration. Direct numerical simulations (DNS) were the first to report quantification of electroconvective flow under unsteady conditions and confirm the presence of chaotic vortices over a range of spatio-temporal scales with broadband spectra[17]. These effects were later quantified for systems similar to the model setup in Figure 1(c), but with additional complexities including imposed inflow[18], induced charge electro-osmosis (ICEO) in which surface conduction over an inert electrode

provides ion-selectivity[19], and patterned surfaces[20]. Most recently, de Valença *et al.*[21] used micro-PIV to quantify chaotic flow fields associated with electroconvection under high voltage. The flow patterns observed in these measurements are consistent with numerical reproduction of PIV performed on DNS using earlier computational methodologies[20]. Until recently, OLC was attributed to sources such as water splitting[22, 23], surface conduction in micropores[24], normal flow into the selective surface[25], and current-induced membrane discharge[26]. Very recently the consensus is that electroconvection plays the dominant role in enhancing mass transport[17, 21] which contributes significantly to OLC. In recent years electroconvection has received considerable attention for its potential to alleviate transport limitation by diffusion.
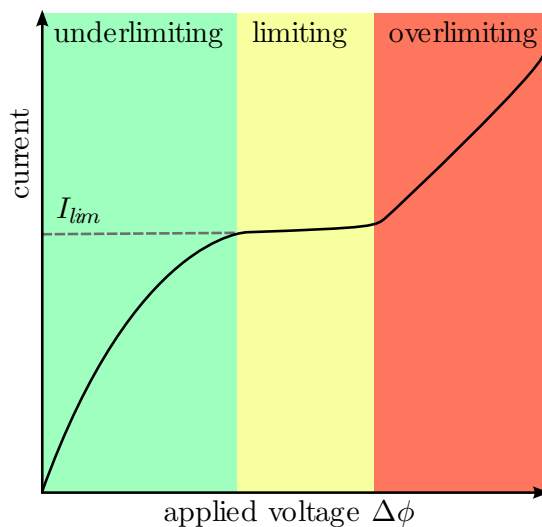
Figure 2. Schematic of the characteristic current-voltage curve for membrane-electrolyte systems.

Experiments with membrane-electrolyte systems exhibit a characteristic current-voltage response with three regimes (Figure 2): the underlimiting regime where the current obeys a linear response[27], the limiting regime where the current plateaus due to concentration polarization[28], and the overlimiting regime where the unexpectedly large increase in current is an ongoing research area[29]. The underlimiting and limiting regimes are well-predicted by one-dimensional models[10] for a stagnant fluid. In the overlimiting regime, however, one-dimensional models significantly underpredict the current density since they fail to capture the effects of electroconvection[11]. Additional 1D models have used experimental current-voltage curves to fit 1D model parameters for improved prediction at overlimiting currents

[30]. However, 1D models are not sufficient for capturing the physics of overlimiting currents.

Here we briefly describe the instability mechanism leading to electroconvection. The key ingredients of this instability are concentration gradients due to concentration polarization and ESC counter charge near the membrane, which can lead to a positive feedback mechanism that amplifies hydrodynamic perturbations. Figure 3 shows a clockwise hypothetical vortex near a cation-selective membrane. The corresponding perturbation to the salt concentration field is shown by tracking an iso-contour of concentration. Due to its low Ohmic resistance, the high concentration zone is expected to have a more uniform potential, and thus a smaller electric field. This means that the imposed downward electric field in the depleted zone will be higher than that in the concentrated zone. Next, we examine the circulation of the electric field around a test loop indicated by the black square in Figure 3. According to the Maxwell-Faraday equation,

$$\oint \mathbf{E} \cdot d\mathbf{l} = 0$$

the circulation of the electric field must be zero. Therefore, a tangential field is induced from right to left near the cation-selective surface to satisfy zero circulation. This tangential field acts on the positively charged ESC layer, producing a body force that induces the clockwise vortex (dashed circle) in the figure. Therefore, the concentration gradients and charge in the ESC create a positive feedback mechanism that amplifies the initial perturbation.
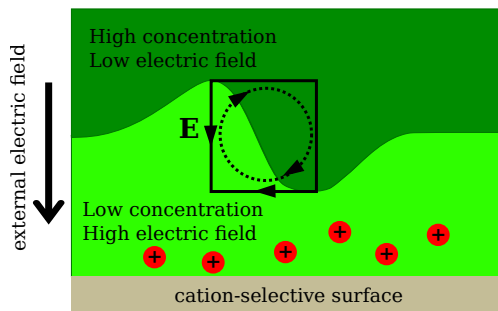
Figure 3. Schematic illustrates the mechanism of the instability. Tangential perturbations lead to an electric field that drive a vortex, amplifying the initial perturbation.

Early models investigating electroconvection have assumed that the concentration boundary layer structure, composed of the EDL and ESC, remains quasi-steady. This assumption has allowed derivation of an asymptotic model that treats the EDL and ESC as an effective

slip boundary condition to an electroneutral bulk over which the transport model should be solved[31]. These models predict steady electroconvective vortices scaled by the domain size. However, recent DNS[17] has revealed that the ESC is highly unsteady, leading to complex vortex structures and an irregular boundary between the ESC and electroneutral bulk. Capturing these detailed dynamics is possible through direct solution to the Poisson-Nernst-Planck and Navier-Stokes (PNP+NS) equations resolving the ESC and EDL structures without relying on any asymptotic approximation.

Aside from first principle calculations which are prohibitively expensive, no theory exists that can accurately predict the current-voltage curve in the OLC regime. Advanced understanding of electroconvection is crucial for the development of models and theories predicting the current-voltage relationship in the overlimiting regime.

In a recent publication[17] we presented 2D simulations of electroconvection via direct solution of the coupled PNP+NS equations that demonstrated transition to chaos revealing the complex structure of the concentration field in various layers. We presented the ensemble-averaged transport equations and quantified the unclosed flux terms associated with correlations of concentration fluctuations with fluctuations of velocity and electric field.

In the current study, we present for the first time analysis of *highly chaotic* electroconvective flows from 3D simulation data. These simulations require very fine resolution, about an order of magnitude higher than those in a previous study[32] that focused on electroconvection close to *transitional regimes*. In contrast to this previous study that reported a diminishing difference in the I-V curve between 2D and 3D fields electroconvection, here we demonstrate that while 2D and 3D fields show qualitatively similar features, the current density of 3D electroconvection is measurably higher than in 2D electroconvection in the high voltage limit.

We also provide a comprehensive statistical analysis of current density on the membrane surface that is subject to chaotic electroconvection. A histogram of current density on the membrane and the temporal spectrum of point-wise current density reveal that significant current is sustained via intermittent "hot spots" of very high current density. Unlike the transitional regime, the instantaneous pattern of the current density does not follow a combination of regular shapes (e.g., hexagons, quadrangles, and triangles) and shows highly irregular patterns. We present joint probability density functions revealing correlation of surface current density with local flow conditions adjacent to the membrane.

Furthermore, we present a detailed comparison between 2D and 3D electroconvection in the highly chaotic regime by investigating a wide range of statistical quantities, including the mean fields and fluxes, and concentration spectra at various distances away from the membrane. We also investigate structures responsible for mixing and show instantaneous snapshots of the mushroom-like plumes of ion-depleted fluid. Large vortices are mainly responsible for bringing ion-rich fluid to the membrane surface and pulling depleted fluid away. Close to the membrane surface, the presence of many small vortices results in a wide range of scales contributing to transport. We present the first quantification of effects of different scales on transport by analyzing the cross-covariance of velocity and concentration fluctuations in the wavenumber space.

The results presented in this study improve understanding of electroconvection on multiple fronts. The analysis of ensemble-averaged fluxes provide guidelines for the development of reduced-order models by highlighting the simplifications that can be made in each asymptotic layer in electroconvective flows. The presented correlation analyses provide guideline for control of electroconvection, by quantifying the importance of various scales and revealing potential mechanisms leading to current hotspots.

II.   MODEL PROBLEM AND GOVERNING EQUATIONS

Realistic electrodialysis systems contain multiple stacks of alternating cation-selective and anion-selective membranes. In this study, we focus on a canonical setting and analyze the transport and dynamical behavior adjacent to a single cation-selective surface. As shown in Figure 1(c), we consider a three-dimensional domain in which an aqueous symmetric binary electrolyte interacts with a cation-selective surface. In this model the bottom boundary represents the cation-selective surface, and we approximate the top boundary as a stationary reservoir that provides anion and cation species at a specified fixed concentration, c_{res}. We consider an external electric field normal to the membrane surface at a sufficiently large voltage ensuring a highly chaotic electroconvective regime.

In this model we assume a symmetric binary electrolyte with the species ionic valence $z = z^+ = -z^-$ and the diffusion coefficient $D = D^+ = D^-$. The governing equations are nondimensionalized by the following characteristic scales

$$t_{diff} = \frac{L^2}{D}, \qquad v_{diff} = \frac{D}{L}, \qquad p_0 = \frac{\mu D}{L^2}, \qquad V_T = \frac{k_B T}{ze}, \qquad j_0 = \frac{D c_{res}}{L} \qquad (1)$$

Table I. Dimensional Parameters and Reference Scales

Input	Description	Reference Scales	Description
L	membrane-to-reservoir distance	V_T	thermal voltage
D	diffusion constant	c_{res}	reservoir concentration
$\Delta\phi$	applied voltage	p_0	pressure scale
μ	dynamic viscosity	t_{diff}	diffusion time
ε	electrical permittivity	v_{diff}	diffusion velocity
z	ionic valence		
e	elementary charge		
k_B	Boltzmann constant		
T	temperature		
ρ	fluid density		

We note that the choice of nondimensionalization does not ensure field variables of $\mathcal{O}(1)$. Table 1 summarizes the dimensional parameters and dimensional scales used to nondimensionalize the governing equations.

The continuum approach is justified as the separation of length scales quantified by the Knudsen number is $Kn \ll 1$. In this case, the Knudsen number is defined as the ratio of the molecular diameter of water (on the order of 1 $\mathring{A}$) to the smallest eddy size (50-500nm for systems with salinity in the range 1-100mM). Validity of continuum approach for the representation of the EDLs has been investigated[33, 34] and is well justified for the concentrations and boundary conditions considered here.

With the given choice of reference scales, the dimensionless mass conservation for the anions and cations is expressed by

$$\frac{\partial c^{\pm}}{\partial t} = -\nabla \cdot \boldsymbol{j}^{\pm} \tag{2}$$

where $c^{\pm}$ represents the concentration of ionic species and $\boldsymbol{j}^{\pm}$, the ionic mass flux vector, is given by the Nernst-Planck equation to describe transport of the ionic species due to advection, diffusion, and electromigration.

$$\boldsymbol{j}^{\pm} = c^{\pm}\boldsymbol{v} - \nabla c^{\pm} \mp c^{\pm}\nabla\phi \tag{3}$$

We consider the incompressible formulation of the Navier-Stokes equations and neglect the nonlinear inertial term which is small compared to the viscous term at Reynolds numbers much less than 1. We retain the unsteady term and note that the Schmidt number $Sc = \mu/(\rho_m D)$ is $\mathcal{O}(10^3)$ in aqueous systems. The dimensionless form of the Navier-Stokes equations are

$$\frac{1}{Sc}\frac{\partial \boldsymbol{v}}{\partial t} = -\nabla p + \nabla^2 \boldsymbol{v} - \frac{\kappa}{2\epsilon^2}(c^+ - c^-)\nabla\phi \tag{4}$$

$$\nabla \cdot \boldsymbol{v} = 0 \tag{5}$$

where v, p, and ϕ represent the velocity vector, pressure, and electric potential fields respectively. Aside from Sc, two other dimensionless parameters include the electrohydrodynamic coupling constant κ,

$$\kappa = \frac{\varepsilon}{\mu D}\left(\frac{k_B T}{ze}\right)^2 \tag{6}$$

and ϵ is the dimensionless EDL size defined by,

$$\epsilon = \frac{\lambda_D}{L}, \quad \lambda_D = \sqrt{\frac{\varepsilon k_B T}{2(ze)^2 c_{res}}} \tag{7}$$

Finally, the relation between electric potential and the charge density is described by the dimensionless form of Gauss' Law,

$$-2\epsilon^2 \nabla^2 \phi = c^+ - c^-. \tag{8}$$

An interesting observation is that here, unlike common turbulent flows, the nonlinearities responsible for chaos are due to electrostatic forces and coupling with ion transport, rather than fluid inertia.

The boundary conditions which uniquely define the system are a cation-selective surface at $y = 0$ with no slip and no penetration for the fluid, grounded electric potential, a no flux condition for anions, and a fixed cation concentration c_0^+,

$$\boldsymbol{v} = 0, \qquad \phi = 0, \qquad j_y^- = 0, \qquad c^+ = c_0^+ \tag{9}$$

The reservoir condition at $y = 1$ is given by no slip and no penetration for the fluid, an applied potential $\Delta\phi$, and fixed cation and anion concentrations,

$$\boldsymbol{v} = 0, \qquad \phi = \Delta\phi, \qquad c^+ = c^- = 1 \tag{10}$$

The domain is periodic in the surface-tangential x and z directions with a domain length of 2π which is sufficiently larger than the correlation length scale in the transverse direction[17] in the range of voltages studied. The domain size in these directions should be much larger than the transverse correlation length to justify physical representation of infinite domain via periodic boundary treatments. In a recent publication, Davidson *et al.*[20] demonstrated that for systems under transitional voltage ($\sim 40V_T$) satisfying this constraint requires simulation domains with very high aspect ratio on the order of $\mathcal{O}(100)$. Prior investigations [32] in the transitional voltage range, used much smaller domain size and are likely to be contaminated by artificial effects of imposing periodic boundary treatments. The present investigation however, is in the highly chaotic high voltage limit; investigations of the correlation length[17], as well as sensitivity of mean transport to the domain size[20] indicate that an aspect ratio of 2π is appropriate for the conditions considered here.

The initial condition is a quiescent flow field and a uniform concentration profile where $c^+ = c^- = 1$. At $t = 0$, the concentration field is subject to a random perturbation of less than 1%. Our simulation captures the full evolution of the physics from the initial transient to the statistically stationary state.

Key dimensionless parameters controlling the flow are summarized in Table II. The critical parameter for the onset of flow instability is the dimensionless applied electric field, $\Delta\phi$. We consider a system at 120 thermal volts which is well into the chaotic regime. We set the value of $\kappa = 0.5$ which is a typical value for aqueous solutions. Furthermore, we consider a dimensionless EDL size, $\epsilon = 10^{-3}$ which is small enough to allow the separation of scales between the EDL size and outer domain, but also large enough to keep the computational cost at a reasonable level. A recent investigation[35] indicated that mean transport rate is only weakly sensitive to ϵ.

III. NUMERICAL PARAMETERS AND COMPUTATIONAL METHODS

The system described by Equations (2)-(5) is a stiff nonlinear system. To obtain an accurate solution, the numerical procedure resolves length scales spanning three orders of magnitude from the extremely thin EDL to the largest scale vortices spanning the distance between the membrane and the reservoir. We use a non-uniform mesh in the y-direction, concentrating mesh points near the membrane with $\Delta y_{\min} = 0.37\lambda_D$ (note that due to

Table II. Dimensionless Parameters

Parameter	Description	Value
$\Delta\phi$	Applied voltage	120
κ	Electrohydrodynamic coupling constant	0.5
ϵ	EDL size	10^{-3}
a	Aspect ratio, $L_x/L = L_z/L$	2π
c_0^+	Cation concentration on ion-selective surface	2
Sc	Schmidt number	1,000

concentration polarization depletion the local EDL size is much thicker than the nominal λ_D). The largest mesh spacing is $\Delta y_{\max} = 14.6\lambda_D$ at the reservoir. Due to statistical homogeneity in the tangential directions, uniform mesh spacing is used in the periodic x and z directions with $\Delta x = \Delta z = 6.5\lambda_D$. We use 165,888,000 mesh points in the 3D volume and adopt a staggered mesh where concentration, electric potential, and pressure are stored on cell centers while velocities, fluxes, and electric field components are stored on cell edges.

A second order time advancement scheme with a time step $\Delta t = 10^{-6}$ is used for the evolution of the concentration and momentum equations. All terms in the governing equations are handled explicitly except for the surface normal electromigration and surface normal diffusion terms. These terms rapidly balance each other near the membrane surface, resulting in formation of the EDL in a quasi-steady manner. The time scale of the chaotic eddies is much larger than the time scale of formation of EDL and thus an appropriate time stepping scheme must use an in-between time step scale that fully resolves the unsteady dynamics while implicitly treating the quasi-steady EDL formation time. Further details on the computational algorithm are described in Karatay *et al.*[36].

IV. INSTANTANEOUS RESULTS

Instantaneous snapshots from the 3D DNS show highly chaotic multiscale vortices that separate and coalesce while interacting in a highly irregular manner (see video in supplementary material). This hydrodynamic behavior leads to concentration depletion plumes shown in Figure 4. Small scale vortices tend to stay close to the membrane surface and are highly active. The resulting fluid motion provides a mixing mechanism for ionic species that
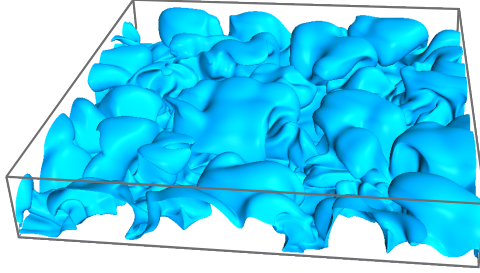
Figure 4. Instantaneous isosurface of total concentration $c = c^+ + c^- = 0.1$.

would otherwise be transported by only electromigration and diffusion.

Figure 5(a) and (b) show instantaneous snapshots from the 2D and 3D simulations that demonstrate many qualitative similarities and exhibit the same range of length scales. Consistent with the 2D simulations, in 3D the chaotic vortices also cause the ESC region to become unsteady and induced vortices disrupt the structure of the ESC. Outside the ESC charge density tends to appear in alternating positive and negative ribbons. We explain how these charge density ribbons are induced through the principles of charge conservation and Gauss' Law. An examination of the data reveals that the charge density ribbons coexist with thin structures (fingers) of depleted concentration as shown in Figure 5(c). When a depletion zone emerges from the ESC, local conductivity gradients occur. To conserve charge the incident electric field adjusts itself in an inversely proportional relationship with the conductivity. Local gradients in the magnitude of the electric field are shown in Figure 5(d).

Next, we consider Gauss Law, equation (8), to determine the expected sign of the induced charge that appears at the interface of the thin depletion fingers. As the electric field passes from a zone of high concentration to low concentration (into a depletion finger), positive charge density will appear. Similarly, as the electric field passes out of a depletion finger (low concentration to high concentration) a zone of negative charge density will appear. This qualitative description corresponds to our observation of paired red/blue ribbons where positive charge is observed on top and negative charge is observed in the bottom of each depletion finger. Charge density ribbons are then advected throughout the domain as the chaotic vortices advect depletion zones.

In regions far away from the ESC, the charge in the ribbons is much smaller than the local concentration and thus the fluid follows a quasi-electroneutral behavior. Ribbons tend
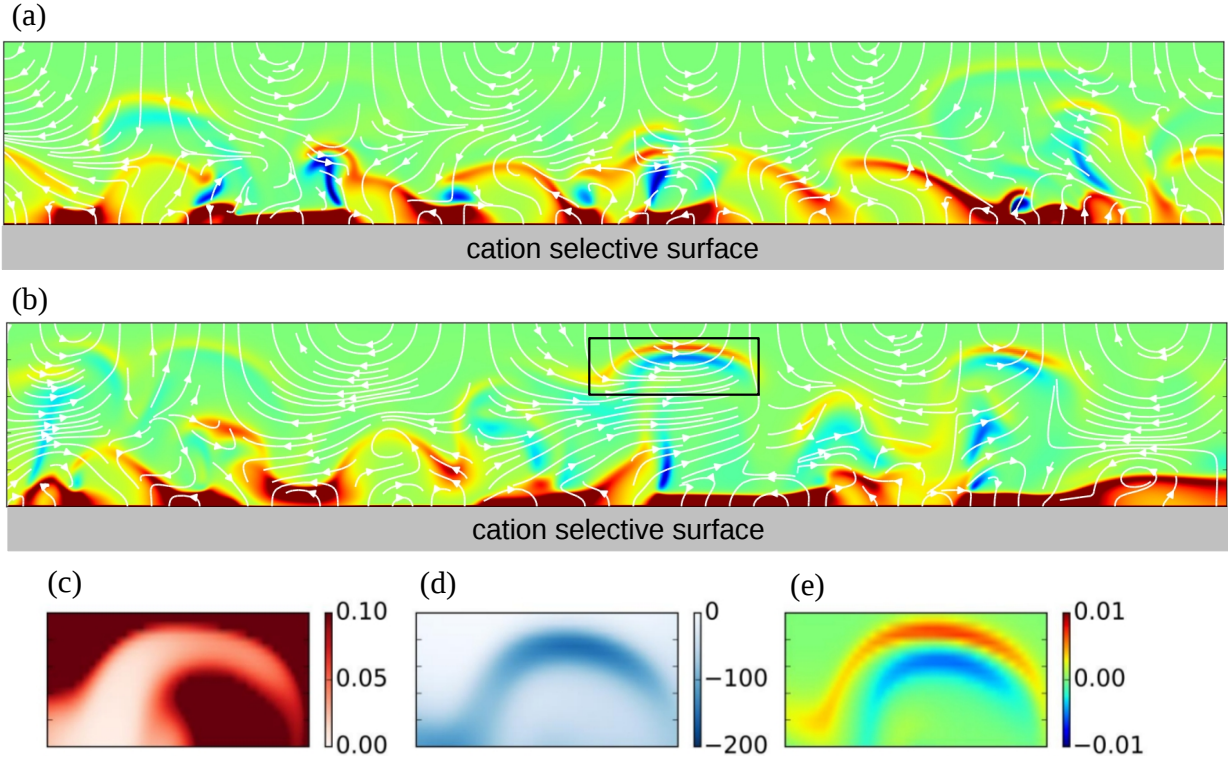
Figure 5. Instantaneous snapshots of charge density $\rho = c^+ - c^-$ with velocity streamlines superimposed from (a) 2D DNS and (b) 3D DNS. The black rectangle highlights a subdomain of the charge density field for further inspection. (c)A thin depletion finger shows sharp gradients in concentration. (d) The magnitude of the induced surface normal electric field. (e) Charge density ribbons.

to align horizontally and normal to the imposed electric field, an observation that can be explained through the primary effects of the electrostatic body force on the induced charge density ribbons. Given the vertical direction of the incident field and the sign of the induced positive and negative charge density from top to bottom, each depletion zone induces a force that squeezes the fluid vertically. By continuity the ribbons and depletion fingers must then stretch horizontally. In regions near the ESC however, these effects are overwhelmed by the strong vortices and by non-electroneutral effects, therefore charge density does not align in a particular orientation.

The qualitative similarities between the 2D and 3D simulations of electroconvection are in contrast to common hydrodynamic instabilities and turbulence phenomena. Specifically, common turbulent flows involve inertial effects and vortex stretching. While vortex stretch-

ing is absent in 2D flows, it plays a significant role in the energy cascade when 3D modes are present. In electroconvection the inertial term in the momentum equation is negligible, and vortex stretching is therefore absent in both 2D and 3D, resulting in a qualitatively similar appearance of the field data. While the qualitative similarities are abundant, as we shall see, the comparison of statistics demonstrate significant quantitative differences in the field data and transport mechanisms between 2D and 3D systems.

V. MEMBRANE STATISTICS

We examine statistics at the cation-selective surface to understand the effect of chaotic dynamics on ionic transport in the overlimiting regime. An instantaneous snapshot of current density on the membrane surface, Figure 6, indicates that the vast majority of the surface area is characterized by low current density with random sparse "hot spots" of high current density. Unlike observations from the transitional voltage regime[32], the current density pattern does not have a regular geometric shape, rather it is highly irregular. Intuitively, it is expected that the current hot spots will occur in regions where high conductivity fluid extends to the membrane since this would provide a direct path for the electric current between the reservoir and the membrane. Consequently, it is expected that these high conductivity regions would extend towards the membrane by advection, since diffusion and electromigration primarily cause CP depletion. Therefore, according to these hypotheses, the membrane normal velocity field in the vicinity of the hot spots should point towards the membrane surface. Prior investigations in the transitional regime[32] showed data fields consistent with these expectations: near the hot spots, normal flow points towards the membrane and, by continuity, tangential flow points away from the hot spot zones forming zones of in-plane divergence.

Figure 6(b) is an example of the in-plane flow field near the membrane to show the relationship between the chaotic flow field and areas of high current density. In contrast to transitional regimes, some of the very high current density regions involve converging tangential flow fields. We will investigate these effects quantitatively in the following sections.

Figure 7(a) shows that the current density highly fluctuates at an arbitrary fixed location on the membrane surface. Hot spots of high current density appear randomly and are short-lived, with a residence time $\Delta t \approx 1 \times 10^{-4}$. In this case the maximum dimensionless
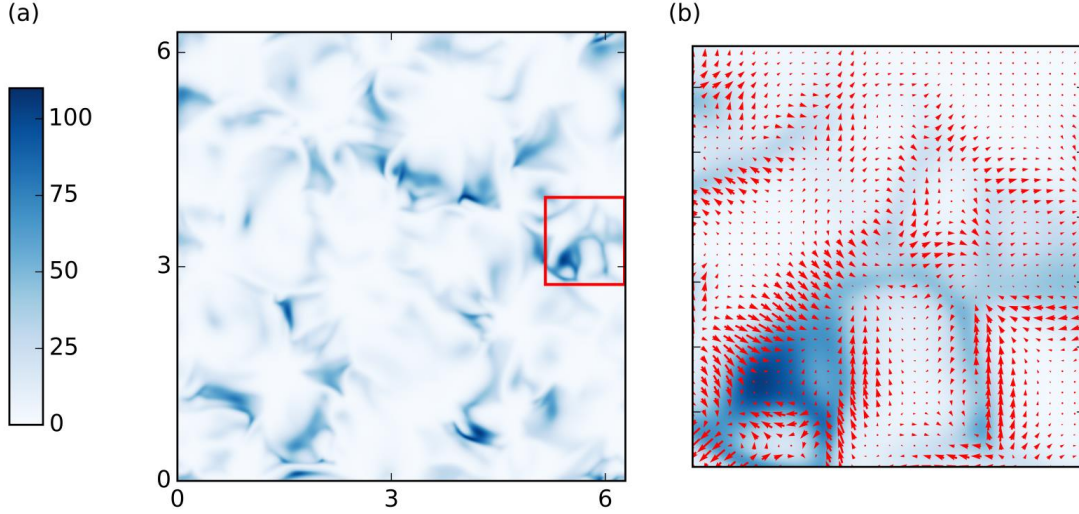
Figure 6. (a) Instantaneous snapshot of current density on the membrane surface. Dark blue indicates areas of high current density. (b) Zoom-in super-imposes velocity vectors near the membrane surface at y = 0.002.

point-wise current density is $i \sim 80$, about 7 times larger than the ensemble-average current density of $\langle I \rangle = 11.2$. This is approximately one third of the maximum possible current density ($i = 240$) that is realizable if the fluid between the reservoir and membrane had a concentration of $c^+ = c^- = 1$.
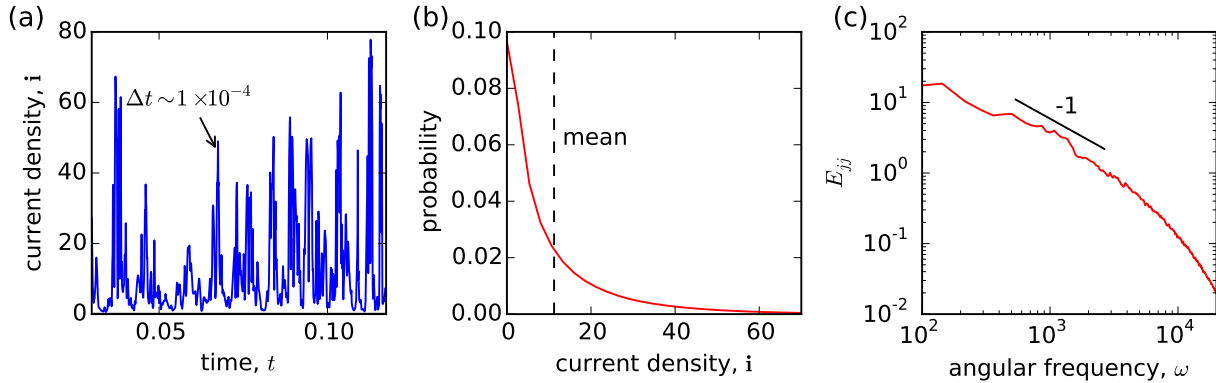
Figure 7. (a) Current density fluctuations at a point on the membrane surface. (b) Histogram of current density on the membrane surface. (c) Temporal spectrum of the current density.

The histogram in Figure 7(b) quantitatively shows that very small current density is the most probable state. Consistent with Figure 7(a), the histogram indicates that any given

point on the membrane surface is at low current density (below the average) most of the time. Sparse spikes in current density therefore make a significant contribution to the mean current density. In some practical applications, such as electrodialysis for desalination, it is desirable to sustain higher current density (i.e., higher desalination throughput) for a given voltage. Understanding the mechanism behind the appearance of hot spots and ultimately developing a method to control and enhance them is of crucial importance[20].

Figure 7(c) shows the temporal spectrum of current density on the membrane surface. Over a wide range of frequencies the spectrum follows a k^{-1} power law, indicating a behavior analogous to Brownian noise. This power law persists up to high frequencies on the order of $\omega \sim 10^4$, indicating that the current density is highly influenced by fast dynamics and in agreement with the short lifespan of hot spots observed in Figure 6(a). Consistent with both observations, visual inspection of the velocity field also shows the complex behavior of vortices that appear to randomly translate in the tangential directions, particularly near the membrane.

VI.   SPECTRAL ANALYSIS

We compute the spatial and temporal spectra to examine how fluctuations in concentration and velocity fields are distributed across the existing length and time scales. By comparing spectra from the 2D and 3D DNS we determine how inclusion of the third dimension changes the statistical behavior of the fields. All of the examined spectra exhibit broadband behavior reminiscent of spectra from high Reynolds number turbulent flows.

Temporal spectra are computed by taking the Fourier transform of field data in time and ensemble-averaging the power spectra in the homogeneous tangential directions. The spectra are then plotted for different y locations. Spatial spectra are computed by taking the Fourier transform of the field data with respect to the tangential (homogeneous) directions and then ensemble-averaging the power spectra over time. For 2D simulations, there is only one homogeneous direction and plotting the spectrum is straight forward. 3D simulations are statistically isotropic in the tangential directions, therefore, the spectra are integrated in the $k_x - k_z$ space over cylindrical shells of constant $k = \sqrt{k_x^2 + k_z^2}$. All spectra are properly computed such that the integral of each spectrum is equal to the variance of the fluctuating quantity.
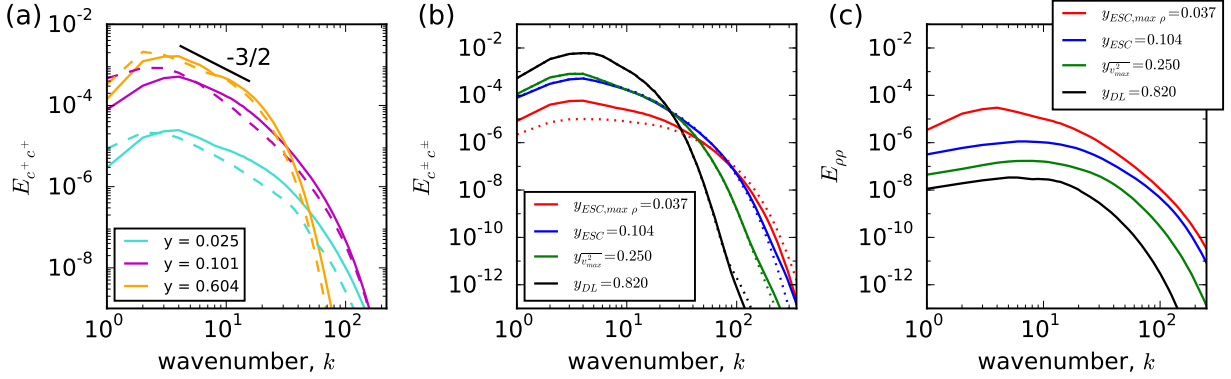
Figure 8. (a) Comparing 2D (dashed) and 3D (solid) spatial spectra of c^+ at multiple surface normal locations. (b) Spatial spectrum of c^+ (solid) and c^- (dotted) from 3D DNS. (c) 3D DNS spatial spectrum of charge density. Refer to Figure 10 regarding the definition of $y_{\text{ESC, max}\,\rho}$, y_{ESC}, $y_{v_{\max}^2}$, y_{DL}.

Figure 8(a) presents spatial spectra for the cation concentration at various y locations for both 2D and 3D simulations. The 3D simulation predicts more energetic behavior across the majority of the wavenumbers particularly near the membrane. The spectra from the 3D simulation indicate up to three times higher energy compared to that from the 2D simulation. However, in regions away from the membrane this difference becomes smaller. Results from the 3D simulation indicate an intermediate wavenumber range with a power law scaling of $k^{-3/2}$.

Figure 8(b) presents the comparison between spatial spectra of cations and anions from 3D simulation data. Outside the ESC spectra from the 2D and 3D simulations are virtually identical with minor deviations at high wavenumbers. This result suggests that away from the ESC the concentration field is likely governed by the quasi-electroneutral approximation. At $y = 0.037$ there is a significant difference between the spectrum of c^+ and c^-. In this region the domain is essentially devoid of c^-. All spectra peak at $k \sim 4$, which corresponds to a dimensional wavelength of $\sim 1.5L$ indicating that fluctuations are dominated by scales on the order of the domain size. However, regions closer to the membrane present spectra that extend further to high wavenumbers, which indicates that higher frequency fluctuations are sustained in this region. This is analogous to observations in turbulent boundary layers. However, in contrast to the boundary layers, the peak intensities in electroconvection spectra

are observed away from the membrane.

Figure 8(c) shows spatial spectra associated with fluctuations of charge, $\rho = c^+ - c^-$, at the same y locations considered in Figure 8(b). Inside the ESC c^- has a negligible presence and the charge spectra is identical to that of c^+. Moving away from the ESC, the fluctuations in charge density drop across all frequencies. This is despite the fact that concentration fluctuations increase further away from the membrane. In other words, the dynamics become increasingly more electroneutral. The peak frequency of charge fluctuations does not correspond to peaks observed in spectra of individual ions. Charge density spectra show peaks at around $k \sim 6 - 8$ which is roughly twice the wavenumber of the peaks in ion concentration. Similar to the concentration spectra, the charge density spectra reach higher frequencies closer to the membrane surface.
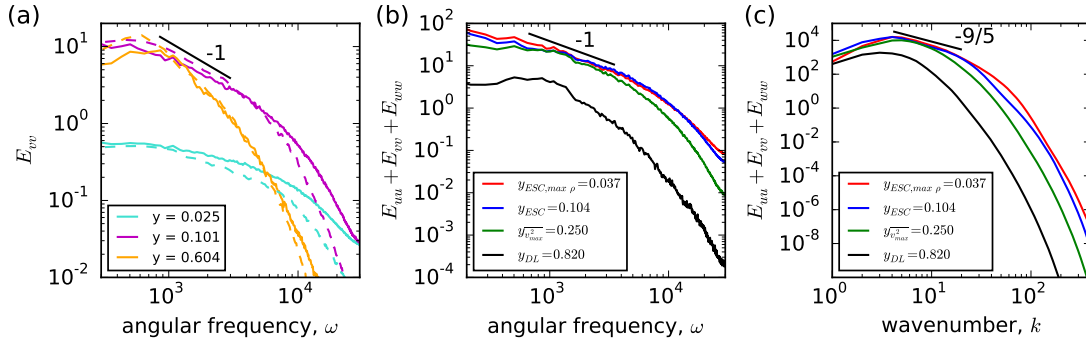
Figure 9. (a) Temporal spectrum of kinetic energy. Comparison of 3D DNS (solid) and 2D DNS (dashed). (b) Temporal spectrum of kinetic energy. (c) Spatial spectrum of kinetic energy.

Next, we present spectral analysis of the velocity field. Figure 9(a) shows the temporal spectrum of the vertical velocity, v, at different distances from the membrane. The v-component contributes to the ensemble-averaged ion mixing, while the other components of the velocity field primarily contribute to dispersing ions in the homogeneous direction. The figure also contrasts the spectra obtained from 2D and 3D simulations. Similar to observations of concentration spectra, the 3D simulations allow for higher fluctuation intensities at large frequencies. Other qualitative trends are similar to observations for concentration spectra as well. However, quantitative differences are expected since momentum transport is dominated by instantaneous diffusion (due to the low Reynolds number) while concentration transport is dominated by advection (due to the high Peclet number).

Figure 9(b) shows the temporal spectra of all three components of the velocity field, representing the distribution of kinetic energy in frequencies. For regions not too far from the membrane, a power law of $E \sim k^{-1}$ emerges for intermediate frequencies. Figure 9(c) shows the corresponding spatial spectra. In this case a power law region is hardly visible, and a line with slope -9/5 is only drawn as a reference. Nevertheless, one can see that the temporal and spatial spectra decay at different rates, and unlike traditional turbulence, Taylor's hypothesis does not hold for electroconvective flows. This is expected since Taylor's hypothesis assumes a strong advective component, while here the momentum field is primarily governed by a Newtonian viscous response to the fluctuating electrostatic body force.

Unlike concentration spectra, the velocity spectra indicate a drop in kinetic energy across all wave numbers for locations away from the membrane. This behavior can be explained by the fact that the electrostatic body force, which is a driver of kinetic energy, is primarily active in regions near the membrane. Kinetic energy attenuates as it diffuses to regions away from zones with the driving body force. The rate of attenuation with distance, is higher for higher wavenumebrs. This observation is explained by the response of the momentum which is mostly governed by the Laplacian operator in the Stokes' flow equation, thus higher frequencies are expected to attenuate exponentially faster, proportional to e^{-ky}. Similar to concentration spectra, the peak intensities are observed for $k \simeq 4$. In other words, both momentum and ion transport are modulated primarily with modes at a scale of roughly $1.5L$.

VII. ENSEMBLE-AVERAGED FIELDS

In this section we present an analysis of the mean field data from 2D and 3D simulations. Additionally, we use the mean concentration fields to identify various regions and important y-locations for this canonical domain setting.

Figure 10(a) shows the ensemble-averaged concentration field, $\bar{c} = \overline{c^+} + \overline{c^-}$ from the 3D DNS. The ensemble average is defined as,

$$\overline{f}(y) = \frac{1}{L_x L_z \tau} \int_{t_0}^{t_0+\tau} \int_0^{L_x} \int_0^{L_z} f(x, y, z, t) \, \mathrm{d}x \mathrm{d}z \mathrm{d}t, \tag{11}$$

where t_0 is the time when the flow has reached fully developed condition and τ is sufficiently larger than the temporal correlation time to allow converged statistical averaging. The
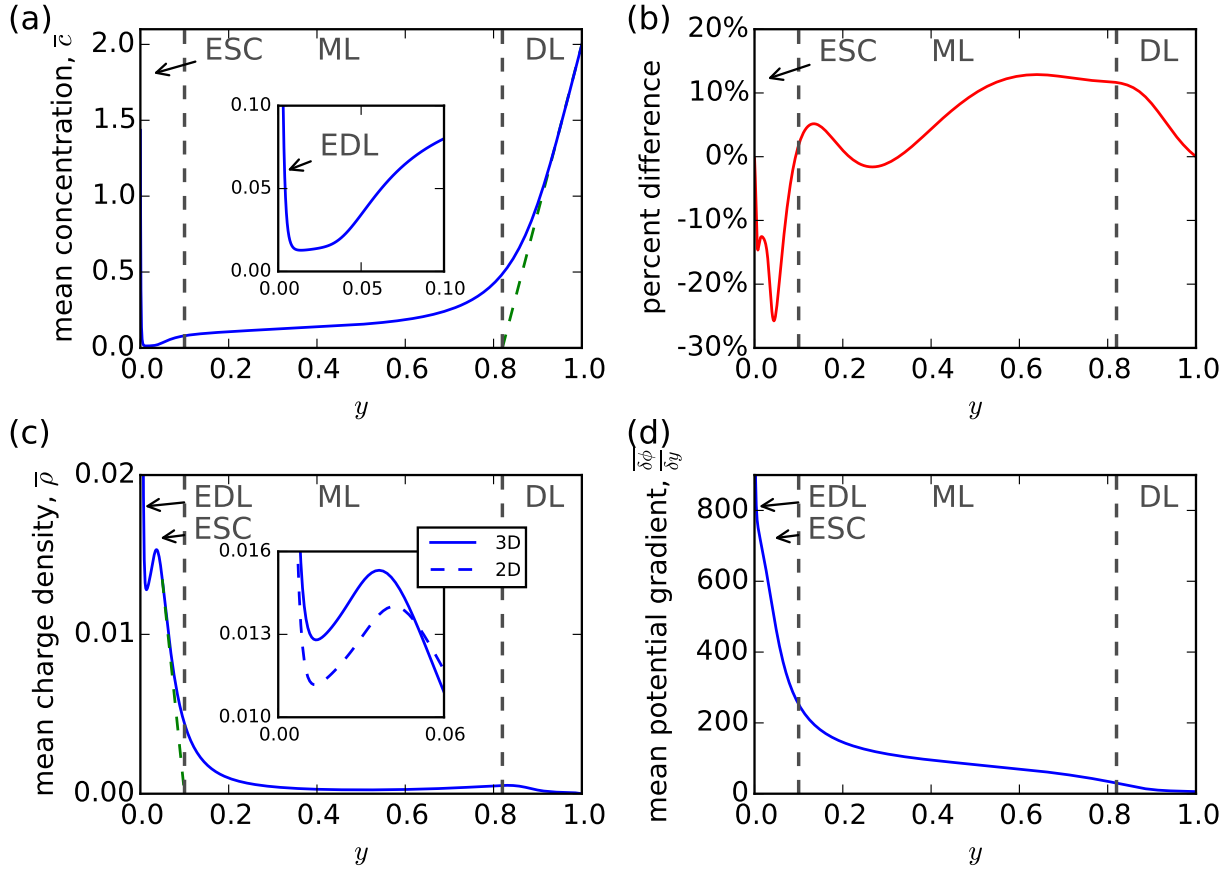
Figure 10. (a) Average total concentration from the 3D DNS. Concentration drops rapidly across the EDL approaching near zero in the ESC. (b) Percent difference between 2D and 3D DNS, with 3D as the reference: $\frac{(\bar{c}_{2D} - \bar{c}_{3D})}{\bar{c}_{3D}} * 100$. (c) Average charge density $\rho = c^+ - c^-$ from 3D DNS. (d) Mean potential gradient as a function of distance from the membrane.

high concentration in the EDL is predominantly composed of cations and rapidly drops to a very small concentration in the ESC. In the 2D DNS we highlighted major impacts of chaotic flow on the mean concentration profile[17]. Many of these qualitative trends are observed in 3D DNS as well. Namely, the ESC is significantly smaller than 1D predictions and the mixing layer (ML) emerges between the ESC and the DL. The ML makes up the majority of the domain and is characterized by a relatively flat concentration profile at moderate values, much smaller than the reservoir concentration but much larger than the ESC concentration. As we shall see in Section IX the advective fluctuations in the ML dominate the net transport. The shrinking of the ESC is explained by the fluctuating eddies that bring high salt concentration fluid from the ML to the membrane at a time scale

comparable to the time scale of ESC formation due to CP.

Near the reservoir, advective fluxes are suppressed due to the no slip boundary condition, and the mean concentration profile is characterized by a relatively constant slope within the DL. The slope of the concentration profile at the reservoir boundary is directly connected to the net current in the system. At the boundary, the advective flux is zero and thus transport is governed by diffusion and electromigration. Given that this region is far away from the ESC, one can use the electroneutral approximation and write the current density as:

$$j = j^+ - j^- = \frac{\partial c}{\partial y}\bigg|_{y=1} \tag{12}$$

Figure 10(b) represents a quantitative comparison between the results of 2D and 3D simulations, by plotting the local percent difference between the two, $\frac{\bar{c}_{2D} - \bar{c}_{3D}}{\bar{c}_{3D}} * 100$. Our results indicate that significant differences of up to 26% are present in the ESC region where the 2D simulation underpredicts the concentration. Even though the ESC is a small region in the domain, prediction of the concentration in this region is critical for correct prediction of net transport. From a circuit model point of view, the ESC acts as a large resistor in series with the rest of the domain, and thus contributes significant impedance against the net current. For the explored setting, the net current through the system is $\langle I \rangle = 11.2$ from the 3D simulation, and $\langle I \rangle = 10.4$ from the 2D simulation. In this setting, the underprediction of concentration in the ESC by the 2D simulation, leads to an overall higher Ohmic resistance in the domain, and thus 7 percent lower electric current. This effect can also be observed by the difference in the slope of concentration near the reservoir, in conjunction with the relation presented in equation (12).

Figure 10(c) shows the mean charge density across the domain. Aside from the EDL, the ESC involves the most significant charge. Similar to 1D solutions[37], the ESC is characterized by a peak in charge density. High charge density persists even beyond the ESC in up to 15% of the distance to the reservoir. However, comparison of Figure 10(a) and 10(c) suggests that the majority of the mixing layer is reasonably electroneutral. The 2D DNS underpredicts the charge density by up to 34%.

Lastly Figure 10(d) shows the mean membrane normal electric field, $-\partial\phi/\partial y$ versus y. As previously discussed, the ESC region has a relatively high electric resistance and requires a higher electric field to sustain the same current as in the ML. The area under the plot represents the potential drop in the domain. One can see that almost half of the potential

drop occurs in the ESC region.

The plots shown in Figure 10, highlight specific y locations, associated with different regions of the system. We define four such locations which are used to track other quantities such as concentration and velocity spectra in Section VI. Starting at the membrane surface, the first location is identified by the peak in mean charge density, $y_{\text{ESC,max}\rho} = 0.037$. The second location, which we refer to as the edge of the ESC, y_{ESC}, is defined based on extension of the line tangent to the inflection point in the charge density profile, shown in Figure 10(c). For the investigated setting, the $y_{\text{ESC}} = 0.104$. The third location, $y_{v^2,\text{max}} = 0.25$ (shown in Figure 12(a)), is defined by the peak in the root-mean-square normal velocity fluctuations. Lastly, the fourth location, $y_{\text{DL}} = 0.82$ highlights the edge of the diffusion layer, and is defined by extending the tangent line to the concentration profile at $y = 1$, as shown in Figure 10(a). The specific values listed here are in general dependent on $\Delta\phi$ and other input parameters. Investigation of multiple DNS data combined with scaling analysis is needed in order to achieve scaling laws for asymptotic dependence of the extent of various layers on the input parameters.

VIII. ENSEMBLE AVERAGED EQUATIONS

We examine the time averaged fluxes corresponding to transport of ions in the system. We first introduce the representation in [17] and considered time-averaged equations for transport of separate species. Then, we demonstrate that this representation can be significantly simplified, when it is derived for total salt given the fact of approximate electroneutrality for the majority of the domain. As presented by Druzgalski et $al.$, the transport equation for ionic species (2) and (3) can be rewritten after ensemble averaging in the following form:

$$\frac{\partial}{\partial y}\left(-\frac{\partial \overline{c}^{\pm}}{\partial y} \mp \overline{c}^{\pm}\frac{\partial \overline{\phi}}{\partial y}\right) + \frac{\partial}{\partial y}\left(\mp \overline{c^{\pm\prime}\frac{\partial \phi\prime}{\partial y}} + \overline{c^{\pm\prime}v\prime}\right) = 0. \tag{13}$$

where the overbar ($\bar{\ }$) symbol represents the ensemble averaged field and the prime symbol, $(\ )\prime$ represents fluctuations relative to the ensemble averaged field. This equation, has two unclosed terms, which are not describable in terms of ensemble-averages of the primary variables. These terms, $\overline{c^{\pm\prime}\frac{\partial \phi\prime}{\partial y}}$ and $\overline{c^{\pm\prime}v\prime}$, respectively represent transport of ions by fluctuating electric field and fluctuating eddies. Figure 11(a) shows the individual electromigration fluxes in equation (13) as well as the total electromigration flux, $\overline{c^{\pm}\frac{\partial\phi}{\partial y}}$. Outside the ESC

the electromigration flux for cations is approximately equal in magnitude, but opposite in sign to the anions for all components of the electromigration flux. This observation confirms that the electroneutrality approximation, $c^+ \simeq c^-$, is highly reasonable in describing fluxes outside of the ESC.

One consequence of this observation is that the total electromigration flux, $\overline{c^{\pm}\frac{\partial \phi}{\partial y}}$ must be relatively constant throughout this subdomain, and equal to half of the net current as seen in Figure 11(a). This consequence is well known from analysis of 1D binary systems[10], and here we briefly rephrase the reason leading to this observation. Given electroneutrality outside of ESC, the diffusive flux and advective fluxes are also equal for cations and anions; these fluxes cancel out the net electromigration flux for anions and sustain the other half of the net current associated with anions.
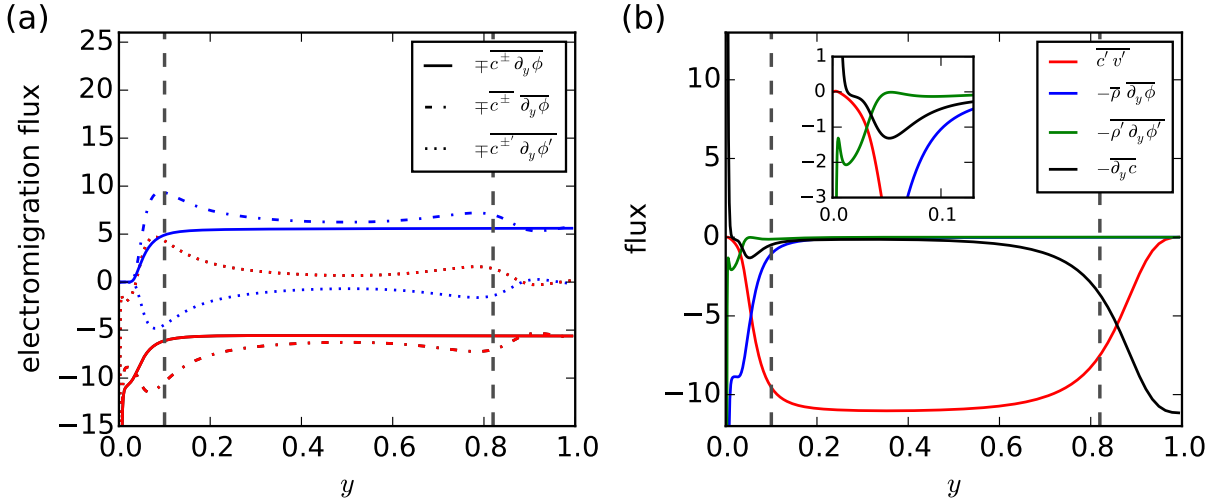
Figure 11. (a)Components of the electromigration flux for $\overline{c^+}$ (red) and $\overline{c^-}$ (blue). (b)Fluxes for transport eqn for $\overline{c} = \overline{c^+} + \overline{c^-}$. All data are presented from 3D simulation.

The observations above motivate analysis of the field data in terms of transport for total salt, c, allowing for approximate cancellation of electromigration fluxes. We present this analysis for chaotic electroconvection here for the first time. The exact transport equation for total salt, c, can be derived by addition the evolution equations for c^+ and c^-:

$$\frac{\partial c}{\partial t} = \nabla \cdot (-\mathbf{u}c + \nabla c + \rho \nabla \phi) \tag{14}$$

Ensemble averaging of this equation leads to the following one-dimensional ordinary differ-

ential equation:

$$\frac{\partial}{\partial y}\left(-\frac{\partial \overline{c}}{\partial y}-\overline{\rho}\frac{\partial \overline{\phi}}{\partial y}\right)+\frac{\partial}{\partial y}\left(-\overline{\rho'\frac{\partial \phi'}{\partial y}}+\overline{c'v'}\right)=0 \tag{15}$$

Figure 11(b) compares all four fluxes as a function of distance from the membrane. At any location these fluxes sum to the net current density through the system, $\langle I \rangle = 11.2$. As expected, outside of ESC both electromigration fluxes are negligible and transport is dominated by mean diffusion and advection by the fluctuating velocity field. The fluctuating electromigration flux is small compared to other fluxes through the majority of the domain, including even a significant portion of the ESC. In the ML it is the advective flux that dominates over all other fluxes. The last observation, implies that the only important unclosed flux is the fluctuating advection flux. This implies that future modeling effort should focus on understanding and capturing this term.
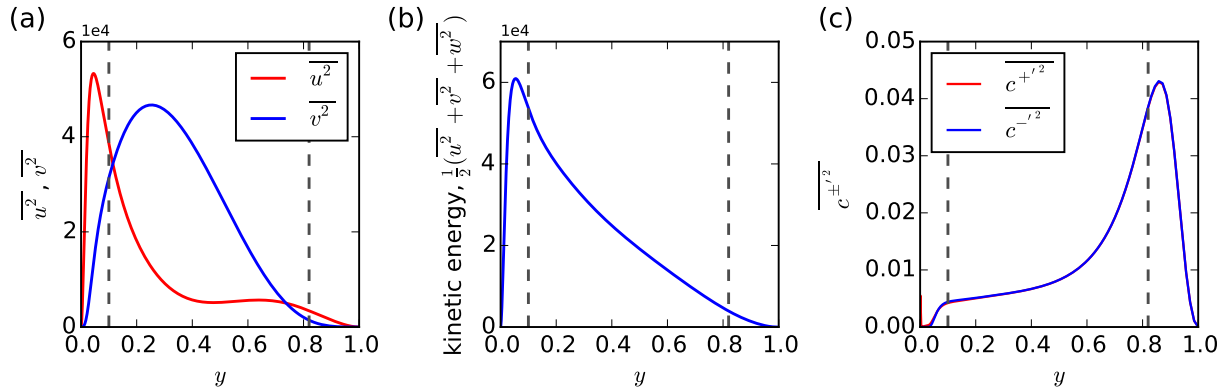
Figure 12. (a) Mean square of tangential (red) and normal (blue) velocity components. (b) mean square of fluctuating kinetic energy in the domain. (c) Mean square of ion concentration as a function of distance to the wall, $\overline{c^{+'2}}$ (red) and $\overline{c^{-'2}}$(blue).All data presented are from the 3D simulation.

Given that the advective flux is governed by fluctuations in both concentration and velocity, next we investigate fluctuations of these quantities in the domain. Figure 12(a) shows velocity variance as a function of y. The variance of the tangential velocity peaks at a location inside the ESC. This is expected because the body force that drives the flow is dominantly confined to within the ESC zone. As explained in Section I, the instability mechanism can generate tangential force near the membrane that would sustain vortices in the domain. The Stokes' flow solution requires that the velocity decays away from the

active forcing zone, as observed in the plot, and as discussed earlier in the analysis of velocity spectra. The variance of the membrane normal velocity component peaks further away from the peak of the tangential component. This is expected, since by continuity the normal component of the velocity must grow slower than the tangential component as one moves away from a no-slip surface. Specifically, within the leading order Taylor series expansion, the normal component grows as $v \sim y^2$ while the tangential component grows as $u \sim y$. Furthermore, the fact that $\overline{v^2}$ peaks outside the ESC indicates that this velocity component is mostly driven by the pressure term to enforce the continuity mismatch associated with in-plane gradients of tangential velocity rather than by the electrostatic body force.

Figure 12(c) shows the variance of concentration field in the domain. The interesting observation is that the concentration variance has its peak near the reservoir boundary, away from the membrane and away from the peak velocity fluctuation zone. We explain this observation based on knowledge from passive scalar transport in turbulent media. The analogy to passive scalars is reasonable here since in the majority of the domain (outside of ESC where concentration is appreciable) the electroneutral assumption is valid and thus one can ignore the last term in equation (14). The production term for variance of scalars[38] is

$$-\overline{c'v'}\frac{\partial \overline{c}}{\partial y} \tag{16}$$

Our explanation for maximum concentration variance near the reservoir is based on the fact that the production term peaks near the reservoir. By inspection, one can see that the production term is indeed the product of the advective flux and diffusive flux in equation (15). The sum of these fluxes is constant throughout most of the domain as shown in Figure 11(b). Therefore, their maximum takes place where the two are equal. Figure 11(b) indicates that the crossing point is at $y = 0.85$; this location corresponds to the peak concentration variance in Figure 12(c).

IX.   TRANSPORT

To explore the mechanisms that contribute to hot spots of high current density observed in Figure 6, we compute joint probability densities between current density i on the surface and other quantities. Based on observations at transitional voltages [32], one hypothesis is that the hot spots correspond to zones where high concentration fluid is advected to the

membrane. Based on this hypothesis one expects to see hot spots correlated with high salt concentration, and velocity towards the membrane. We explore these correlations in Figure13. Figure 13(a) shows the joint PDF of current on the membrane surface and c^- at $y = 0.1$. The reason to not use c^+ for the investigation of correlation, is because cation concentration is highly influenced by the EDL on the membrane as well as by electromigration in the ESC. c^- is the species whose high concentration near the membrane can only be sustained by advection. We considered a location further away from the membrane to compute the correlation, since c^- is exponentially small very near the membrane, and thus we considered a location on the edge of the ESC to be more appropriate for this study. Likewise, for investigation of correlations with other quantities we considered locations near but not exactly on the membrane surface. According to Figure13(a), the presence of high c^- in the near-membrane region, does not guarantee that a hot spot will form on the membrane surface. However, there is a weak positive correlation between high current density on the membrane and high local concentration. In Figure 13(b) the joint PDF of current density on the membrane and gradient in potential near the surface is well correlated. One interpretation is that at the hot spots, there is a path from reservoir to the membrane in the bulk fluid that involves an overall small resistance. Therefore, most of the electrostatic drop happens near the membrane, which inevitably involves extreme depletion. In other words, the correlation presented in Figure13(b) is better than that in Figure 13(a), because it takes into account both the local concentration effects and the entire path for current to pass from reservoir to membrane.

In Figure 13(c) the surface normal velocity and current density do not show a strong correlation, however note that high current density (80 and above) is only possible with a negative normal velocity. This implies that pockets of high current density are associated with locations where the flow advects the fluid towards the membrane surface. The fact that the presented correlations are weak, do not perfectly clarify the mechanism of hot spots. Here we present that the sign of correlations match the intuitive expectations but further research is needed for full characterization of hot spots and understanding of the mechanisms responsible for their formation.

Last, we address the question of the scales that contribute most to advective transport.
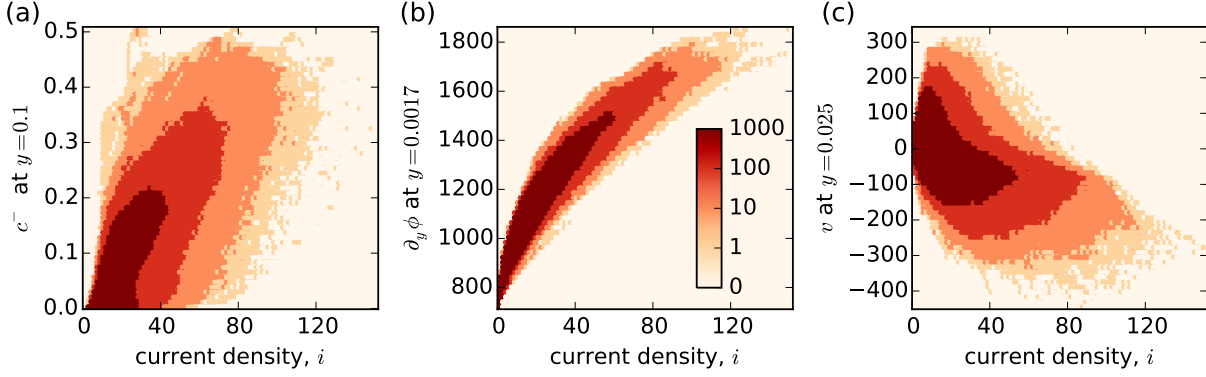
Figure 13. (a) Joint PDF of current density and c^-. (b) Joint PDF of current density and potential gradient indicates a strong correlation: large gradients are associated with high current density. (c) Joint PDF of current density and v shows that high current density is only correlated with velocity into the membrane.

We compute the spectrum of $v'c'$ defined as:

$$E_{v'c'}(y,k) = \frac{1}{2\tau}\left(\frac{L}{\pi N_x N_z}\right)^2 \int_0^\pi \int_{t_0}^{t_0+\tau} \hat{c}^* \hat{v}'(k_x, y, k_z) dt d\theta \qquad (17)$$

where $\hat{()}$ is the 2D discrete Fourier transform and $()^*$ is the complex conjugate. Like other presented spectra, we integrate this spectrum over cylindrical shells in the $k_x - k_z$ plane. The resulting plot represents a decomposition of $\overline{v'c'}$ in terms of wavenumbers (scales). Figure 14(a) shows such spectra corresponding to different y locations. The negative numbers on the y-axis indicate that the corresponding scales contribute to transport from reservoir to the membrane. Positive numbers indicate a counter gradient transport from membrane to the reservoir. For regions outside of the ESC, the spectra reach the most negative value at the wavenumber $k \simeq 4$. This indicates that in these regions, transport to the membrane is mostly controlled by large eddies $\lambda = \frac{2\pi}{k} \simeq 1.5L$. This is not surprising since, as shown in Figure 8 and Figure 9, the most energetic fluctuations for both concentration and velocity fields are associated with the same wavenumber. In the regions within the ESC however, the spectrum has a broadband flat region indicating a wider range of scales contribute to the net transport. Again, this is consistent with earlier observations indicating the presence of small vortices near the membrane.

Some of the presented spectra are positive for a portion of the wavenumbers indicating a counterintuitive salt transport from membrane to the reservoir. While this type of transport

does not happen in the time averaged sense ($\overline{v'c'}$ is negative for all y's) locally such effects can occur. For example, in Figure 14(b), we show a mushroom structure generated as a result of the growth of depletion fingers away from the membrane. The velocity field points away from the membrane on the main depletion branch, but once one of the extended depletion fingers overturns, the velocity field transports a region of low concentration back to the membrane. In other words, particularly on thin extended fingers, it is possible to achieve transport against the mean gradient of concentration.
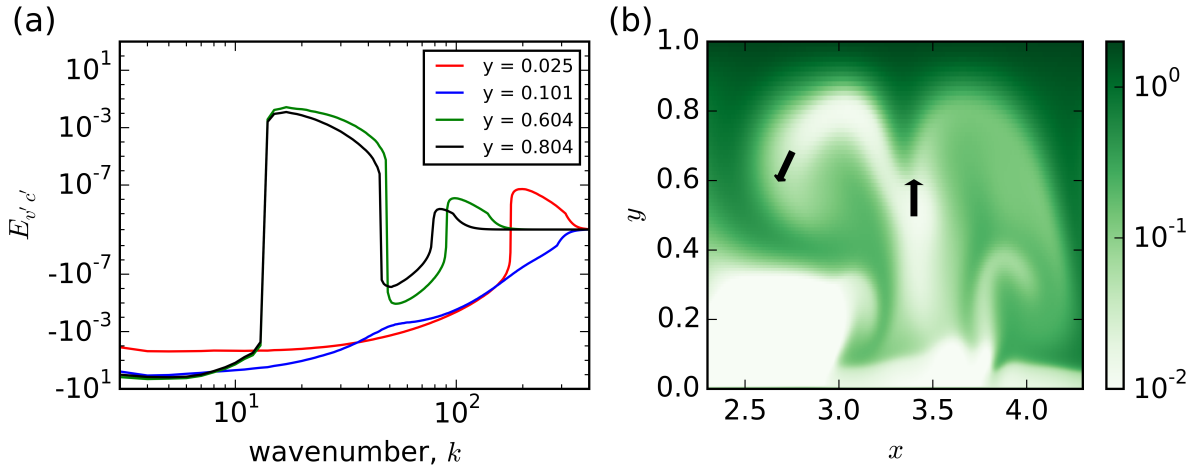
Figure 14. (a) Spectrum of $v'c'$ for different y locations. (b) Concentration field with arrows indicating the direction of the velocity field. Presented results are from 3D DNS data.

X. CONCLUSION

The presented results contribute to the advancement of understanding electroconvection in the highly chaotic regime and quantitative characterization of the phenomena that contributes to OLC. Specifically, we considered electroconvection at an applied voltage of $\Delta\phi = 120$ which is well into the highly chaotic regime. An examination of instantaneous snapshots from 2D and 3D DNS show many qualitative similarities. Inertial turbulence demonstrates qualitative difference between 2D and 3D fields, which is attributed to the presence of vortex stretching in 3D flows. However, electroconvection is a low Reynolds number phenomenon, and thus vortex stretching is absent both in 2D and 3D. Despite these qualitative similarities, the quantitative prediction of mean quantities such as concentration,

charge density, and current density show significant discrepancies between 2D and 3D. The affects of dimensionality on the quantitative prediction, particularly in the ESC where the body force and kinetic energy are largest, highlight the need for full 3D DNS calculations.

Instantaneous snapshots of current density on the membrane surface reveal the appearance of high-intensity yet short-lived current density hot spots. Statistical analysis shows that the majority of the membrane surface is characterized by relatively low current density, while the hot spots contribute significantly to the mean current density. We compute joint PDFs of current density on the membrane and other quantities to explore the mechanism that causes hot spots. Understanding this mechanism and ultimately developing a method to control and enhance it has many favorable engineering applications, such as increasing the throughput in electrodialysis systems. The computed correlations match intuitive expectations such as the appearance of high current density correlated with a velocity field towards the membrane surface. Although the presented analysis indicates positive correlations, these correlations are not very strong. Therefore, further research is needed to fully characterize the mechanisms leading to hot spots.

The spatial and temporal spectra of quantities such as concentration, charge density, velocity, and kinetic energy were computed and showed broadband behavior reminiscent of spectra from high Reynolds number turbulent flows. The spatial spectra of concentration showed up to 3 times higher fluctation intensity in 3D than in 2D over a wide range of wavenumbers. Both the concentration and kinetic energy spectra from 3D data show a peak at $k \sim 4$ indicating that both momentum and ion transport are modulated primarily with modes at a scale of roughly $1.5L$.

We derived an ensemble-averaged one-dimensional ODE with two unclosed terms and used the 3D data to compute the time averaged fluxes that contribute to transport of ions. We determined that the only important unclosed flux term is the fluctuating advection flux and thus modeling efforts should focus on this term. Furthermore, our analysis revealed that transport in the ML can be well approximated by an electroneutral model; in the ML the fluctuating advection flux is the only important term.

Lastly, we assessed the importance of different scales on the advective transport by examining cross-correlations between concentration and velocity fluctuations in the wavenumber space. Transport to the membrane is mostly controlled by large eddies, however in the ESC a wider range of scales contribute to net transport due to the presence of small vortices near

the membrane.

The research presented here can be extended in multiple directions. First, even within the considered simplified canonical setting the trends in transport and dependence of the nested boundary layers (EDL, ESC, ML, DL) on the input parameters is still an unsolved problem. Many more DNS simulations are needed to allow for a general quantitative characterization of the regimes and their coupling. Second, development and verification of a reduced order model is crucial to extend these developments to practical engineering applications. The presented ensemble-averaged equation is one framework for the development of such models. Lastly, extending the analysis of electroconvection to non-ideal scenarios is a natural next step. Such extensions may include complex geometry[20], imposed flow[18], complexity of the electrolyte and coupling with non-equlibrium chemistry[39], and non-ideal membranes[40].

---

[1] Pourcelly, Nikonenko, Pismenskaya, and Yaroslavtsev. Ionic Interactions in Natural and Synthetic Macromolecules Ch. 20, 2012.

[2] K.N. Mani. Electrodialysis Water Splitting Technology. *Journal of Membrane Science*, 58:117–138, 1991.

[3] Scott, K. Handbook of Industrial Membranes. pages 725–769. Elsevier, 2nd edition, 1998.

[4] Edwin Vera, Jacqueline Sandeaux, Francoise, Persin, Pourcelly, Gerald, Dornier, Manuel, and Ruales, Jenny. Deacidification of clarified tropical fruit juices by electrodialysis. Part I. Influence of operating conditions on the process performances. *Journal of Food Engineering*, 78:1427–1438, 2007.

[5] Adam Z. Weber, Matthew M. Mench, Jeremy P. Meyers, Philip N. Ross, Jeffrey T. Gostick, and Qinghua Liu. Redox flow batteries: a review. *Journal of Applied Electrochemistry*, 41(10):1137–1164, October 2011.

[6] Dongyang Chen, Shuanjin Wang, Min Xiao, and Yuezhong Meng. Preparation and properties of sulfonated poly(fluorenyl ether ketone) membrane for vanadium redox flow battery application. *Journal of Power Sources*, 195(7):2089–2095, April 2010.

[7] Li-Jing Cheng and L. Jay Guo. Ionic Current Rectification, Breakdown, and Switching in Heterogeneous Oxide Nanofluidic Devices. *ACS Nano*, 3(3):575–584, March 2009.

[8] Matthew E. Suss, Ali Mani, Thomas A. Zangle, and Juan G. Santiago. Electroosmotic pump

performance is affected by concentration polarizations of both electrodes and pump. *Sensors and Actuators A: Physical*, 165(2):310–315, February 2011.

[9] Ping Wang, Zilin Chen, and Hsueh-Chia Chang. A new electro-osmotic pump based on silica monoliths. *Sensors and Actuators B: Chemical*, 113(1):500–509, January 2006.

[10] V.G. Levich and D.B. Spalding. *Physicochemical Hydrodynamics*. Prentice-Hall, 1962.

[11] F Maletzki, H.W. Rosler, and E. Staude. Ion transfer across electrodialysis membranes in the overlimiting current range: stationary voltage current characteristics and current noise power spectra under different conditions of free convection. *Journal of Membrane Science*, pages 105–115, 1992.

[12] S. Rubinstein, G. Manukyan, A. Staicu, I. Rubinstein, B. Zaltzman, R. Lammertink, F. Mugele, and M. Wessling. Direct Observation of a Nonequilibrium Electro-Osmotic Instability. *Physical Review Letters*, 101(23), December 2008.

[13] Sung Kim, Ying-Chih Wang, Jeong Lee, Hongchul Jang, and Jongyoon Han. Concentration Polarization and Nonlinear Electrokinetic Flow near a Nanofluidic Channel. *Physical Review Letters*, 99(4), July 2007.

[14] Gilad Yossifon and Hsueh-Chia Chang. Selection of Nonequilibrium Overlimiting Currents: Universal Depletion Layer Formation Dynamics and Vortex Instability. *Physical Review Letters*, 101(25), December 2008.

[15] Sung Jae Kim, Sung Hee Ko, Rhokyun Kwak, Jonathan D. Posner, Kwan Hyoung Kang, and Jongyoon Han. Multi-vortical flow inducing electrokinetic instability in ion concentration polarization layer. *Nanoscale*, 4(23):7406, 2012.

[16] Rhokyun Kwak, Guofeng Guan, Weng Kung Peng, and Jongyoon Han. Microscale electrodialysis: Concentration profiling and vortex visualization. *Desalination*, 308:138–146, January 2013.

[17] C. L. Druzgalski, M. B. Andersen, and A. Mani. Direct numerical simulation of electroconvective instability and hydrodynamic chaos near an ion-selective surface. *Physics of Fluids*, 25(11):110804, 2013.

[18] Van Sang Pham, Zirui Li, Kian Meng Lim, Jacob K. White, and Jongyoon Han. Direct numerical simulation of electroconvective instability and hysteretic current-voltage response of a permselective membrane. *Physical Review E*, 86(4), October 2012.

[19] Scott M. Davidson, Mathias B. Andersen, and Ali Mani. Chaotic Induced-Charge Electro-

Osmosis. *Physical Review Letters*, 112(12), March 2014.

[20] Scott M. Davidson, Matthias Wessling, and Ali Mani. On the Dynamical Regimes of Pattern-Accelerated Electroconvection. *Scientific Reports*, 6:22505, March 2016.

[21] Joeri C. de Valença, R. Martijn Wagterveld, Rob G. H. Lammertink, and Peichun Amy Tsai. Dynamics of microvortices induced by ion concentration polarization. *Physical Review E*, 92(3), September 2015.

[22] Carl-Ola Danielsson, Anders Dahlkild, Anna Velin, and Mårten Behm. A model for the enhanced water dissociation on monopolar membranes. *Electrochimica Acta*, 54(11):2983–2991, April 2009.

[23] R. Simons. Strong electric field effects on proton transfer between membrane-bound amines and water. *Nature*, 280:824–826, 1979.

[24] E. Victoria Dydek, Boris Zaltzman, Isaak Rubinstein, D. S. Deng, Ali Mani, and Martin Z. Bazant. Overlimiting Current in a Microchannel. *Physical Review Letters*, 107(11), September 2011.

[25] Aditya S. Khair. Concentration polarization and second-kind electrokinetic instability at an ion-selective surface admitting normal flow. *Physics of Fluids*, 23(7):072003, 2011.

[26] M. B. Andersen, M. van Soestbergen, A. Mani, H. Bruus, P. M. Biesheuvel, and M. Z. Bazant. Current-Induced Membrane Discharge. *Physical Review Letters*, 109(10), September 2012.

[27] Elena I. Belova, Galina Yu. Lopatkova, Natalia D. Pismenskaya, Victor V. Nikonenko, Christian Larchet, and Gerald Pourcelly. Effect of Anion-exchange Membrane Surface Properties on Mechanisms of Overlimiting Mass Transfer. *The Journal of Physical Chemistry B*, 110(27):13458–13469, July 2006.

[28] R.F. Probstein. *Physicochemical Hydrodynamics: An Introduction*. John Wiley & Sons, 1994.

[29] Victor V. Nikonenko, Anna V. Kovalenko, Mahamet K. Urtenov, Natalia D. Pismenskaya, Jongyoon Han, Philippe Sistat, and Gérald Pourcelly. Desalination at overlimiting currents: State-of-the-art and perspectives. *Desalination*, 342:85–106, June 2014.

[30] Mahamet A.-Kh. Urtenov, Evgeniya V. Kirillova, Natalia M. Seidova, and Victor V. Nikonenko. Decoupling of the Nernst Planck and Poisson Equations. Application to a Membrane System at Overlimiting Currents. *The Journal of Physical Chemistry B*, 111(51):14208–14222, December 2007.

[31] Isaak Rubinstein and Boris Zaltzman. Electro-osmotically induced convection at a permselec-

tive membrane. *Physical Review E*, 62(2):2238, 2000.

[32] E. A. Demekhin, N. V. Nikitin, and V. S. Shelistov. Three-dimensional Coherent Structures of Electrokinetic Instability. *arXiv preprint arXiv:1402.2889*, 2014.

[33] Mustafa Sabri Kilic, Martin Z. Bazant, and Armand Ajdari. Steric effects in the dynamics of electrolytes at large applied voltages. I. Double-layer charging. *Physical Review E*, 75(2), February 2007.

[34] Jonathan W. Lee, Ali Mani, and Jeremy A. Templeton. Atomistic and Molecular Effects in Electric Double Layers at High Surface Charges. *Langmuir*, 31(27):7496–7502, July 2015.

[35] Elif Karatay, Mathias Bækbo Andersen, Matthias Wessling, and Ali Mani. Coupling between Buoyancy Forces and Electroconvective Instability near Ion-Selective Surfaces. *Physical Review Letters*, 116(19), May 2016.

[36] Elif Karatay, Clara L. Druzgalski, and Ali Mani. Simulation of chaotic electrokinetic transport: Performance of commercial software versus custom-built direct numerical simulation codes. *Journal of Colloid and Interface Science*, 446:67–76, May 2015.

[37] Ehud Yariv. Asymptotic current-voltage relations for currents exceeding the diffusion limit. *Physical Review E*, 80(5), November 2009.

[38] Stephen Pope. *Turbulent Flows*. Cambridge University Press, 2000.

[39] Mathias B. Andersen, David M. Rogers, Junyu Mai, Benjamin Schudel, Anson V. Hatch, Susan B. Rempe, and Ali Mani. Spatiotemporal pH Dynamics in Concentration Polarization near Ion-Selective Membranes. *Langmuir*, 30(26):7902–7912, July 2014.

[40] Robert Femmer, Ali Mani, and Matthias Wessling. Ion transport through electrolyte/polyelectrolyte multi-layers. *Scientific Reports*, 5:11583, June 2015.